



# Photocatalytic Glycerol Conversion and Rhodamine B Degradation: Influence of TiO<sub>2</sub> Properties by Transformation of Anatase and Rutile Phases

Igor Mateus de Amorim Silva · Geovânia Cordeiro de Assis · Cristian José Giertyas · Janaína Heberle Bortoluzzi · Tiago Gomes dos Santos · Mario Roberto Meneghetti · Simoni Margareti Plentz Meneghetti 

Received: 2 April 2023 / Accepted: 13 May 2023 / Published online: 31 May 2023  
© The Author(s), under exclusive licence to Springer Nature Switzerland AG 2023

**Abstract** TiO<sub>2</sub> was synthesized by precipitation method at different calcination temperatures and characterized. Materials exhibiting diverse surface, structural and surface properties were obtained and evaluated in the photodegradation of rhodamine B (RhB) dye, and the photocatalytic conversion of glycerol. The increase in the calcination temperature caused a decrease in the surface area (109.0, 69.0, 9.0, and 5.0 m<sup>2</sup>/g for TiO<sub>2</sub>-350, TiO<sub>2</sub>-550, TiO<sub>2</sub>-750, and TiO<sub>2</sub>-950, respectively) and a transformation of anatase to rutile phase. For the photodegradation of RhB, the photocatalytic efficiency was 58.6, 62.8, 31.7, and 16.5% for TiO<sub>2</sub>-350, TiO<sub>2</sub>-550, TiO<sub>2</sub>-750, and TiO<sub>2</sub>-950, respectively. The n-deethylation was improved using TiO<sub>2</sub>-350 (higher surface area) and chromophore cleavage appeared to improve when mixed anatase–rutile crystal-line phases of TiO<sub>2</sub> were identified. For the photocatalytic conversion of

glycerol, the surface area was a determining factor in increasing the conversion with photocatalytic efficiency was 20.5, 15.6, 10.8, and 6.6% for TiO<sub>2</sub>-350, TiO<sub>2</sub>-550, TiO<sub>2</sub>-750, and TiO<sub>2</sub>-950, respectively, but the TiO<sub>2</sub> phase transformation proved to be important for the selectivity and yield of the identified products. The results obtained emphasize the vital role of investigations of photocatalysts for advanced studies on formation of by-products from the n-deethylation of rhodamine B. Furthermore, no similar studies using TiO<sub>2</sub> synthesized by the precipitation method for photocatalytic conversion of glycerol were related, even though this is an important innovation for obtaining products of industrial interest under mild reaction conditions.

**Keywords** Photodegradation · Photocatalytic conversion; Titanium dioxide · Rhodamine B · Glycerol

I. M. de Amorim Silva · C. J. Giertyas ·  
J. H. Bortoluzzi · T. G. dos Santos · M. R. Meneghetti ·  
S. M. P. Meneghetti (✉)  
Group of Catalysis and Chemical Reactivity,  
Institute of Chemistry and Biotechnology, Federal  
University of Alagoas, Av. Lourival de Melo Mota,  
57072-970 Maceió, AL, Brazil  
e-mail: simoni.plentz@gmail.com

G. C. de Assis  
Research Group in Advanced Oxidative Processes (AdOx),  
Department of Chemical Engineering, Escola Politécnica,  
University of São Paulo, Av. Professor Luciano Gualberto,  
05508010 São Paulo, SP, Brazil

## 1 Introduction

During the last decades, investigations on metal oxides have been increasing (Scheinost, 2005), since they have unexpected properties and peculiar and varied applications, such as sensors (Yoon et al., 2022), catalysts (Mavuso et al., 2022), adsorbents (Rahim et al., 2023; Tuzen et al., 2018), fuel cells (Lv et al., 2022), among others. In catalysis, metal oxides have received increasing attention as photocatalysts in

the degradation of hazardous contaminants (Abdullah et al., 2022), photoelectrochemical oxidation of water (Yin et al., 2022) CO<sub>2</sub> conversion (Zhang et al., 2019a, 2019b) hydrogen production (Lee et al., 2022) and conversion of biomass into chemical inputs of industrial interest (Torres-Olea et al., 2020). A photocatalyst is defined as a material with characteristics of a semiconductor, which is capable of absorbing light, producing electron–hole pairs that allow chemical transformations (Khan, 2018; Li & Li, 2017), and metal oxides such as V<sub>2</sub>O<sub>5</sub> (Chauhan et al., 2022), Cr<sub>2</sub>O<sub>3</sub> (Zelekew et al., 2021), ZrO<sub>2</sub> (Helmiyati et al., 2022), ZnO (Franco et al., 2022) SnO<sub>2</sub> (Aihemaiti et al., 2022), MoO<sub>3</sub> (Xue et al., 2019), CeO<sub>2</sub> (Iqbal et al., 2021), Bi<sub>2</sub>O<sub>3</sub> (Sharma et al., 2022), WO<sub>3</sub> (Shandilya et al., 2022), ZnS (Hojamberdiev et al., 2020),  $\alpha$ -Fe<sub>2</sub>O<sub>3</sub> (Araujo et al., 2021), SiO<sub>2</sub> (Joseph et al., 2021), and TiO<sub>2</sub> (Li et al., 2022; Ullah et al., 2023), are excellent candidates for photocatalysis. In order to increase their photoactivity, the properties surface, structural, electronic, morphological of materials having these features have all been intensively researched in photocatalytic systems.

TiO<sub>2</sub> is an excellently chemically stable n-type semiconductor with tunable electrical characteristics (Lazau et al., 2021), widely used in solar cells (Noori et al., 2022), antibacterial agents (Ouerghi et al., 2021), and in self-cleaning coatings (Gonciarz et al., 2021). In addition to these uses, photocatalytic reactions involving TiO<sub>2</sub> have been thoroughly studied (Giraldo-Aguirre et al., 2015; Hu et al., 2022). Anatase, rutile, and brookite are the three polymorphs of TiO<sub>2</sub> that are known (Zhang et al., 2014). The most significant and extensively researched phases to photocatalysis are rutile and anatase (Vequizo et al., 2017), since anatase exhibits important photocatalytic activity (Zhang et al., 2014) and rutile has great stability (Miah, 2021). TiO<sub>2</sub>-anatase has a band gap of 3.2 eV (Zhang et al., 2014) that is considered wide, and thus absorbs mainly in the UV region. Additionally, one of the advantages of TiO<sub>2</sub>-anatase is its small grain size, resulting in high surface area (Yuangpho et al., 2015). In contrast, TiO<sub>2</sub>-rutile has a slightly lower band gap energy of the ~3.0 eV (Zhang et al., 2014), has good stability, but is known to have a large grain size, which gives this material a very low surface area. Furthermore, TiO<sub>2</sub>-rutile has a high rate of electron–hole recombination (Reitz et al., 2014). Numerous research demonstrate that it is wise to

generate TiO<sub>2</sub> with a biphasic anatase–rutile structure in order to reduce internal electron–hole pair (e<sup>-</sup>/h<sup>+</sup>) recombinations while still producing a material that is visible light active (Hu et al., 2018). In this way, the photocatalytic efficiency can be increased due to interfacial charge transport from the junction between the rutile and anatase phases during photoexcitation, which inhibits anatase charge recombination; this leads to efficient separation of photogenerated electron–hole pairs and increased photocatalytic activity (Singh et al., 2019). Mixing phases is known to have synergistic effects and increased photocatalytic activity compared to pure phases (He et al., 2019). By adjusting the calcination temperature, it is possible to produce the mixed anatase–rutile phase structure (Kim et al., 2021; Phromma et al., 2020). The energy band locations of the various TiO<sub>2</sub> phases are different in the mixed phase, and electrons are moved from the anatase phase to the rutile phase. Commercial TiO<sub>2</sub>, with an anatase–rutile biphasic structure is an example and is always selected as the reference photocatalyst due to its high photocatalytic activity, however, commercial TiO<sub>2</sub> is prepared by a flame-powered vapor aerosol technology, where special complex equipment is required, and phase relationships are difficult to control (Zhang et al., 2019a, 2019b).

TiO<sub>2</sub> crystalline phase, particle size and shape, surface area, and degree of crystallinity all affect its physical and chemical properties (Santos et al., 2021). In addition to the influence of the calcination temperature, these factors may vary according to the synthesis method adopted (Payormhorm et al., 2017). The most reported synthesis routes for obtaining TiO<sub>2</sub> are sol–gel (Mushtaq et al., 2020), microwave assisted hydrothermal (Li et al., 2021), and precipitation (Buraso et al., 2018). Synthesis by precipitation is one of the most accessible methods to obtain mesoporous oxides, providing high surface area and particle homogeneity (Muniandy et al., 2017); high yield is one of the main advantages of this method (Bodke et al., 2018).

The literature has already reported numerous investigations with TiO<sub>2</sub> in photocatalytic processes for various applications, including photodegradation of hazardous textile dyes, such as rhodamine B, methylene blue, among others (Xu and Ma, 2021; Domínguez-Jaimes et al., 2021). However, the search for multifunctional TiO<sub>2</sub>-based materials for photocatalysis is extremely relevant. Furthermore,

photocatalysis has received considerable attention in an innovative application that has grown in recent years, which is the conversion of biomass into chemical inputs of high added value (Jin et al., 2017; Roongraung et al., 2020).

A green and renewable substitute for fossil fuels is biodiesel, but its production yields a significant amount of crude glycerol, causing a glut on the market, as only a small amount of this glycerol can be used as fuel or transformed into other chemicals (Çetinkaya et al., 2022; Zhao et al., 2019). Glycerol hydroxyl groups are known to assist its conversion into a number of crucial industrial compounds such as glyceraldehyde (GAD), glycolic acid (GCOA), 1,3-dihydroxyacetone (DHA), glyceric acid (GCA), lactic acid (LA), formic acid (FA), tartaric acid (TA), among others (Zhao et al., 2019; Imbault & Farnood, 2020). Usually, the conversion of glycerol is carried out under severe reaction conditions, such as alkaline conditions, high temperature and pressures, and the deactivation of the catalyst used (Jedsukontorn et al., 2018). With these obstacles, in recent years there has been a need to find a new green process to meet the growing demands of sustainable technologies and clean energy (Maurino et al., 2008). Heterogeneous photocatalysis has been considered one of the most attractive processes due to its superior characteristics, such as being environmentally benign, high efficiency, operation at room temperature and atmospheric pressure (Jedsukontorn et al., 2018). Since 2008, when Maurino et al. (2008) first investigated the photocatalytic transformation of glycerol into high value-added inputs, several other investigations have further supported the efficiency of this reaction system based on heterogeneous photocatalysis using different photocatalysts (Jedsukontorn et al., 2018; Limpachanangkul et al., 2022; Zhao et al., 2019).

Verifying the relationship between the calcination temperature, with the surface, electronic and structural properties is a strategic exploration for the manufacture of multifunctional materials applied in the degradation of organic contaminants, as well as applied to the conversion of plant biomass derivatives into chemical inputs of high added value. In the study reported here, the precipitation method was used to synthesize  $\text{TiO}_2$  with different heat treatment temperatures. By photocatalytic converting glycerol into compounds of industrial interest and the dye Rhodamine B (RhB) photodegradation, the produced

materials were characterized and their photocatalytic properties were assessed. An extensively used reaction model called a closed system was employed to conduct the reactions. This study sought to establish a link between the anatase and rutile phases of  $\text{TiO}_2$  and a combination of the two phases and the materials' photocatalytic effectiveness. It also sought to evaluate the impact of heat treatment temperature on the characteristics of  $\text{TiO}_2$ . It is important to highlight that  $\text{TiO}_2$  is a photocatalyst widely applied in photocatalytic processes; however, no previous reports were found that relate the influence of the increase in calcination temperature with the conversion of glycerol, and in the selectivity of formation of certain products of industrial interest. Also, despite the photobleaching of RhB being frequently investigated in heterogeneous photocatalysis, here we suggest that, in fact, a photodegradation of RhB occurs, and this was identified by the detection of less toxic by-products than the RhB molecule. Furthermore, the results show that the formation of these by-products occurs through the n-deethylation of RhB.

## 2 Experimental

### 2.1 Synthesis of $\text{TiO}_2$

$\text{TiO}_2$  was synthesized using the precipitation method, as described by Cassaignon et al., 2007 with adaptations. Titanium trichloride ( $\text{TiCl}_3$  15%-Vetec, Rio de Janeiro, Brazil), was used as a starting material for the preparation of  $\text{TiO}_2$ . In the procedure, a 1 M solution of  $\text{TiCl}_3$  was prepared, and under vigorous stirring, 10 mL of Ammonium Hydroxide was slowly dripped ( $\text{NH}_4\text{OH}$ - Dinâmica, São Paulo, Brazil), or until reaching  $\text{pH} \cong 8.5$ . The solution was maintained by continuous stirring for 60 min, where it was observed that the solution changed from a purple color to a bluish violet color, which soon evolved to a gray color. At the end of this step, the white precipitate was formed, after which the appropriate washings were carried out in order to eliminate chloride ions from the precipitate. Posteriorly, drying was carried out in an oven at  $80^\circ\text{C}$  for 16 h, then the material was macerated and sieved and then calcinations were carried out at 350, 550, 750, and  $950^\circ\text{C}$ , and named as  $\text{TiO}_2$ -350,  $\text{TiO}_2$ -550,  $\text{TiO}_2$ -750, and  $\text{TiO}_2$ -950.

## 2.2 Characterization of Photocatalysts

The materials were analyzed by X-ray diffraction (XRD) (Shimadzu, model Rigaku Multiflex diffractometer, Kyoto, Japan), in the Bragg angle range of  $2\theta=2-80^\circ$  with a step of  $0.02^\circ$ . With the Scherrer equation it was possible to estimate the crystal size (Arfaoui et al., 2018). The adsorption–desorption measurements of nitrogen were carried out at 77.15 K (Quantachrome analyzer, model Nova 2200e, Moscow, Russia). The textural properties were estimated using the Brunauer–Emmett–Teller equation (BET). The Fourier transform infrared (FTIR) spectra were obtained on a Shimadzu IR Prestige 21 equipment, Kyoto, Japan, from pellets mounted with KBr. The measurement parameters occurred in the middle infrared region ( $4000-400\text{ cm}^{-1}$ ) in transmittance, 65 scans and resolution of  $4.0\text{ cm}^{-1}$ . Raman spectroscopy of photocatalysts was performed at  $\sim 30^\circ\text{C}$  using a 532-nm laser, 10 mW power,  $100\times$  objective, and 16 data acquisitions in 120 s with respect to silica, (HORIBA Scientific equipment, model XploRA, New Jersey, EUA). The spectra in the ultraviolet and visible (UV–Vis) region were obtained on a Shimadzu, model UV-2600, Kyoto, Japan. The measurements were made in absorbance in the interval of 200–800 nm and resolution of  $8\text{ cm}^{-1}$ .

The absorption spectra obtained in the UV–Vis were used to quantify the band gap energy of the photocatalysts (Eq. 1). As a result, Tauc graphs (Wood & Tauc, 1972; Murphy, 2007). Were constructed of  $(\alpha h\nu)^2$  as a function of photon energy (eV), where  $\alpha$  corresponds to the absorption coefficient,  $h$  is the Planck constant, and  $\nu$  is the wavenumber. In addition, in Eq. 1,  $A$  is a constant and  $E_g$  is the band gap energy ( $n=1/2$  for a direct band gap and  $n=2$  for an indirect band gap) (Murphy, 2007).

$$\alpha h\nu = A(h\nu - E_g)^n \quad (1)$$

## 2.3 Photocatalytic Performance

### 2.3.1 Rhodamine B Photodegradation

We prepared an aqueous solution of rhodamine B ( $1.25\times 10^{-5}\text{ mol L}^{-1}$ ) with 4.5 mg of photocatalyst in 15 mL of the dye solution. Then, the solution was poured into 20 mL closed vials and a cooling jacket was

applied at a constant temperature of  $30^\circ\text{C}$ . This system remained under agitation, with a light source composed of four 15 W lamps (Phillips Amsterdam, Netherlands) emitting UV-A light ( $\sim 360\text{ nm}$ ;  $\sim 3.44\text{ eV}$ ), inside a closed wooden chamber with syringes attached on the outside. Initially, the samples were kept in the dark for 60 min to ensure the adsorption/desorption equilibrium of rhodamine B on the catalytic surface. Right after, irradiation was propagated on the samples for 70 min, totaling a reaction time of 130 min. During the irradiation period, aliquots (0.5 mL) were collected every 10 min, centrifuged for 5 min at 5000 rpm, and finally analyzed by spectrophotometry. In addition, photolysis reactions were also carried out, where the experiments were conducted in the absence of photocatalysts and in the presence of UV-A light. These reactions were performed in triplicate and the samples were stored properly to avoid exposure to light. The absorption spectra in the UV–Vis region (200–800 nm) were obtained in a Shimadzu spectrophotometer, model UV-2600, Kyoto, Japan, and the wavelength chosen for analysis was recorded at 554 nm (De Assis et al., 2018). The percentage of rhodamine B photodegradation was calculated based on Eq. 2, where,  $C_0$  is the initial concentration of methylene blue and  $C_t$  is the concentration after the time of irradiation ( $t$ ).

$$\text{Photodegradation(\%)} = \frac{C_0 - C_t}{C_0} \times 100\% \quad (2)$$

### 2.3.2 Glycerol Photocatalytic Conversion

All photocatalytic tests for glycerol conversion were performed in a reactor with the configuration described above (for photodegradation of RhB). The glycerol solution (5 mM) was prepared in Milli-Q water. For the reaction, 7 mL of glycerol solution (5 mM) were used, the catalyst concentration was 5 g/L, 0.5 mL aliquots were collected at pre-established times of 30, 60, 90 and 120 min, and filtered through  $0.45\text{ }\mu\text{m}$  Millipore filters to remove particulate matter from the photocatalyst prior to high performance liquid chromatography (HPLC) analysis. The conversion of glycerol and the products formed were monitored using CTO-20A HPLC system fitted with an RID-10A (Shimadzu, Kyoto, Japan), model pump PopStar 210 (Varian), 20  $\mu\text{L}$  injection volume. The separation was carried out in a stainless-steel H plus column ( $300\text{ mm}\times 7,8\text{ mm d.i.}$ ;

MetaCarb), operating under the following conditions: column temperature at 39 °C, mobile phase was Milli-Q water/phosphoric acid (pH:2.2), with a flow rate of 0.40 mL/min. The products detected were quantified using calibration curves obtained from standards.

The glycerol conversion was calculated using Eq. 3, in which  $C$  (%) = glycerol conversion,  $C_0$  = initial concentration of glycerol ( $\text{mol.L}^{-1}$ ), and  $C_f$  = final concentration of glycerol.

$$C(\%) = \left( \frac{C_0 - C_f}{C_0} \right) \times 100 \quad (3)$$

The yields and selectivities were calculated according to Eqs. 4 and 5, respectively, where  $Y_i$  (%) = yield of product  $i$ ,  $C_i$  = concentration of product  $i$  ( $\text{mol.L}^{-1}$ ),  $C_0$  = initial concentration of fructose ( $\text{mol.L}^{-1}$ ),  $S_i$  (%) = selectivity to product  $i$ , and  $C_{i1}$ ,  $C_{i2}$ ,  $C_{i3}$ ,  $C_{i4}$ ,  $C_{i5}$  = concentrations of various products formed ( $\text{mol/L}$ ).

$$Y_i(\%) = C_i / C_0 \times 100 \quad (4)$$

$$S_i(\%) = \left( \frac{C_i}{C_i + C_{i2} + C_{i3} + C_{i4} + C_{i5}} \right) \quad (5)$$

### 3 Results and Discussion

#### 3.1 Characterization of Photocatalysts

The XRD patterns for  $\text{TiO}_2$  prepared and calcined at different temperatures (range of 350–950 °C for 5 h)

are shown in Fig. 1. For  $\text{TiO}_2$ -350 and  $\text{TiO}_2$ -550, the formation of the anatase phase (JCPDS 21–1272) can be observed, which is confirmed by the presence of crystallographic planes [101], [004] and [200] at  $2\theta = 25.28$ , 37.81, and 48.05° (Khanam & Rout, 2022). The transformation of anatase to rutile phases was pronounced in  $\text{TiO}_2$ -750, where, in addition to the planes referring to the anatase phase, according to the crystallographic sheet JCPDS 21–1276 it is possible to identify crystallographic planes referring to the rutile phase of  $\text{TiO}_2$  at [110], [101], [200], [111], [210], [211] and [220] in  $2\theta = 27.43$ , 36.08, 39.18, 41.22, 44.10, 54.32, and 56.63° (Lal et al., 2021). These results are in agreement with those observed by Byrne et al. (2016), and Sienkiewicz et al. (2021), where the transition from the anatase phase to the rutile phase occurred at temperatures above 600 °C. At 950 °C, the complete transformation of the anatase phase to rutile occurs, and the presence of sharp peaks suggests that the crystallinity of  $\text{TiO}_2$ -950 is very high, and these results are in line with previous investigations (Selman & Husham, 2016; Shah & Rather, 2021a 2021b).

Using the Debye–Scherrer equation (Arfaoui et al., 2018), the average crystallite size ( $D_c$ ) was determined from the two most intense diffraction peaks, [101] for anatase and [110] for rutile. The results are shown in Table 1. With an increase in the calcination temperature,  $\text{TiO}_2$  crystallite size may be seen to grow (Sienkiewicz et al., 2021; Shah & Rather, 2021b). As seen in Fig. 1, the diffractograms still show that  $\text{TiO}_2$  calcinated at low calcinating temperatures (<550 °C),

**Fig. 1** X-ray diffractograms obtained for  $\text{TiO}_2$ -350,  $\text{TiO}_2$ -550,  $\text{TiO}_2$ -750 e  $\text{TiO}_2$ -950

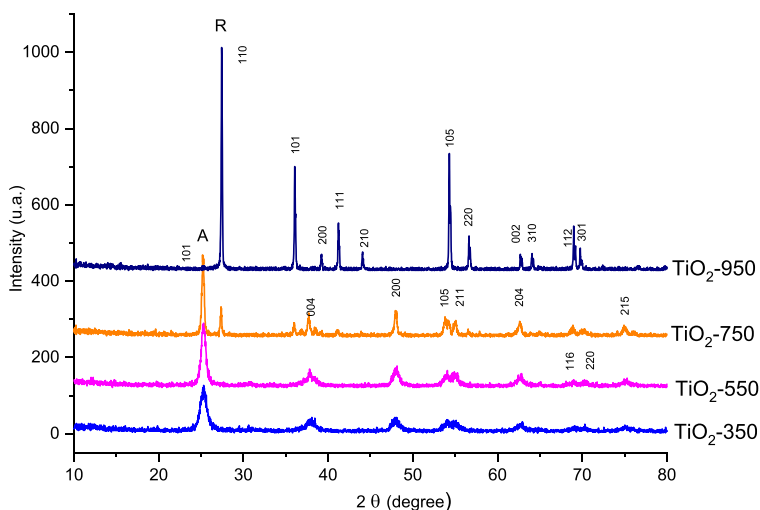


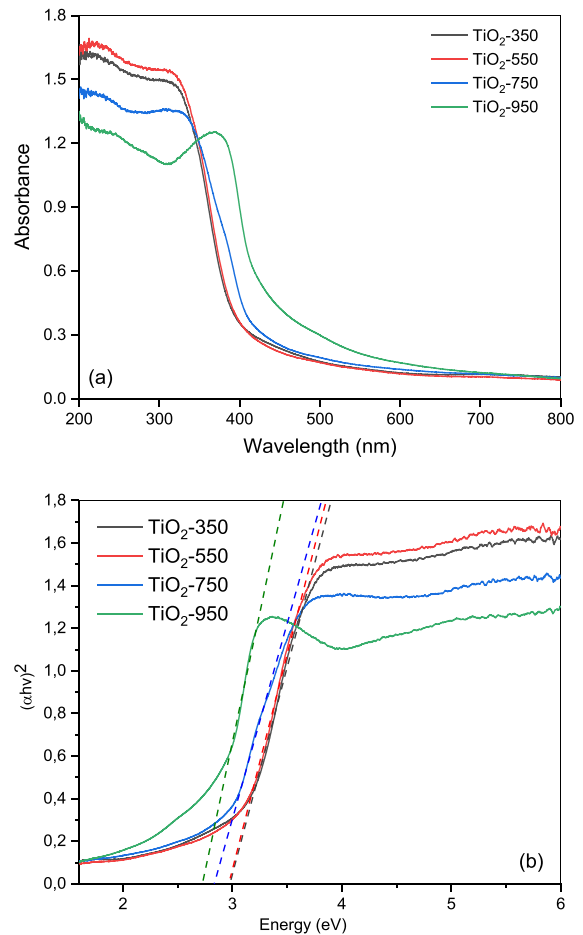
**Table 1** TiO<sub>2</sub> calcined at various temperatures has variable textural and structural characteristics

Samples	$D_c$ (nm) <sup>a</sup>	$E_g$ (eV) <sup>b</sup>	$S_{BET}$ <sup>c</sup>
TiO <sub>2</sub> -350	9.89	3.0	109.0
TiO <sub>2</sub> -550	13.61	2.9	69.0
TiO <sub>2</sub> -750	23.66 (Anatase) 40.22 (Rutile)	2.8	9.0
TiO <sub>2</sub> -950	55.06	2.7	5.0

<sup>a</sup>  $D_c$  = average crystallite size, <sup>b</sup>  $E_g$  = band gap energy, <sup>c</sup>  $S_{BET}$  = BET specific surface area

exhibit large XRD peaks, due to the amorphous structure of TiO<sub>2</sub>, leading to smaller crystallite size. As the calcination temperature increases (> 550 °C), the XRD peaks narrow and increase continuously, influenced by the increase in crystallite size (Kim et al., 2021), as shown in Table 1. This can be attributed to the elimination of crystallite defects during the calcination at high temperatures (Kim et al., 2021; Choudhury & Choudhury, 2013). The anatase to rutile phase transition depends significantly on the size of the crystallites. Anatase has a more stable thermodynamic equilibrium at low temperatures, and when the annealing temperature rises, the grain expands and uses less energy total as a result. The rutile phase is created when the Ti–O bonds are ruptured and reorganized octahedrally at high annealing temperatures, which causes the anatase phase to collapse and reduce the total energy (Sarngan et al., 2022). The calcination process can inevitably cause a decline in surface area, and the results show that the surface area decreased with increasing temperature (Kim et al., 2021; Sienkiewicz et al., 2021) (see Table 1). This can be attributed to a rise in particle aggregation, which speeds up the growth of crystallite size (Sienkiewicz et al., 2021).

It is well-known that a semiconductor's ability to absorb light is connected to its photocatalytic activity (Cai et al., 2016). Using diffuse UV–vis reflectance spectroscopy (DRS), the samples optical and electronic characteristics were investigated (DRS). Figure 2.a and 2.b shows the DRS spectra and Tauc graphs for TiO<sub>2</sub>-350, TiO<sub>2</sub>-550, TiO<sub>2</sub>-750, and TiO<sub>2</sub>-950. The UV–vis absorption spectra of the TiO<sub>2</sub> in Fig. 2.a clearly show that the UV–vis absorption edge is shifted toward higher wavelengths with an increase in calcination (Kim et al., 2021). According to Saikumari et al. (2021) and Geetha et al.

**Fig. 2** (a) UV–Vis diffuse reflectance spectra and (b) Tauc plots for TiO<sub>2</sub>-350, TiO<sub>2</sub>-550, TiO<sub>2</sub>-750, and TiO<sub>2</sub>-950

(2018), this bathochromic shift (red shift), might be due to the delocalization of molecular orbitals in the least unoccupied conduction band of semiconducting metal oxides. The redshift of the absorption edge may also be related to the narrowing of the bandgap, because of the transformation of the anatase to rutile phase in annealing (Morawski et al., 2021). This is in accordance with the observation from the XRD measurements. Using the Tauc method (Table 1), which extrapolates the linear section of the graph  $(\alpha h\nu)^2 \times h\nu$  to yield the energy of the gap value, the  $E_g$  was calculated from the absorption spectra (see Fig. 2.b) (Wood & Tauc, 1972; Murphy et al., 2007). Band gap energy values are represented in Table 1. The estimated band gap values for TiO<sub>2</sub> calcined at different temperatures range from 2.7 and 3.0 eV (the

band gap of  $\text{TiO}_2$ -950 (2.7 eV) is smaller than that of  $\text{TiO}_2$ -350 (3.0 eV). It is observed that the optical gap clearly decreases with the calcination temperature (Geetha et al., 2018; Kamarulzaman et al., 2019), and these results can be explained based on particle size, which affects the optical gap. This may be connected to the effect of quantum confinement, which causes an increase in the band gap because fewer orbitals are involved in the production of the valence band (BV) and conduction band (BC) through orbital overlap, hence reducing the number of orbitals that contribute to the band gap. A larger gap is therefore expected for lower particle sizes (Bera et al., 2010).

Raman spectroscopy investigate of all solids for  $\text{TiO}_2$  treated at various calcination temperatures was performed to further investigate the transition of  $\text{TiO}_2$  phases (see Fig. 3). This method is a crucial tool for identifying the surface defects in the photocatalysts (Kar et al., 2010). From the group factor analysis, there are five active Raman modes for the anatase phase of  $\text{TiO}_2$  ( $3E_g$ : 144, 197, e 639  $\text{cm}^{-1}$  +  $1A_{1g}$ : 513  $\text{cm}^{-1}$  +  $B_{1g}$ : 399  $\text{cm}^{-1}$ ) and four modes for the rutile phase ( $1B_{1g}$ : 143  $\text{cm}^{-1}$  +  $1E_g$ : 447  $\text{cm}^{-1}$  +  $1A_{1g}$ : 612  $\text{cm}^{-1}$  +  $1B_{2g}$ : 826  $\text{cm}^{-1}$ ) (Kalaivani & Anilkumar, 2017; Gao et al., 2014). For the  $\text{TiO}_2$ -350 and  $\text{TiO}_2$ -550 samples, five Raman signals were identified at 144, 200, 398, 519 e 643  $\text{cm}^{-1}$ , which are assigned to the anatase phase modes  $E_g$ ,  $E_g$ ,  $B_{1g}$ ,  $A_{1g}$  e  $E_g$ , respectively (Gao et al., 2014; Fathi-Hafshejani et al., 2020).

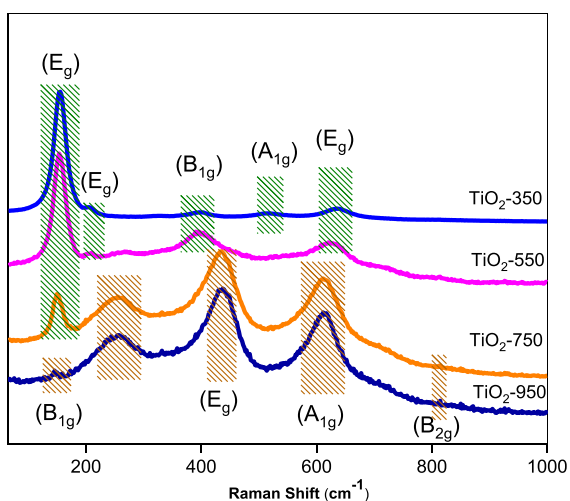


**Fig. 3** Raman spectra obtained for  $\text{TiO}_2$ -350,  $\text{TiO}_2$ -550,  $\text{TiO}_2$ -750 e  $\text{TiO}_2$ -950

It was observed that as the temperature increased from  $\text{TiO}_2$ -350 to  $\text{TiO}_2$ -550, there was an intensification of the signs of these modes. For  $\text{TiO}_2$ -750, the presence of a mixed anatase–rutile phase is verified, with the beginning of a transition from the anatase to rutile phase being observed, which is confirmed by the decrease of the  $E_g$  signal at 143  $\text{cm}^{-1}$  for the anatase phase, and identification of the Raman signals in 447, 612 and 826  $\text{cm}^{-1}$  that are attributed to the rutile phase modes  $E_g$ ,  $A_{1g}$  and  $B_{2g}$ , respectively. For  $\text{TiO}_2$ -950, there is no evidence of modes related to the anatase phase, and the rutile phase increases as evidenced by growing signal intensity at 143, 477, 612 e 826  $\text{cm}^{-1}$  referring to the modes of the rutile phase  $B_{1g}$ ,  $E_g$ ,  $1g$ ,  $B_{2g}$ . For samples  $\text{TiO}_2$ -550 and  $\text{TiO}_2$ -750, a wide band was observed around 250  $\text{cm}^{-1}$ , which is characteristic of the contribution of the non-zero tensor impact on the second-order phonon (Kalaivani et al., 2017; Porto et al., 1967; Padmini et al., 2021). The results agree with the XRD spectra.

The FT-IR spectra were registered in the range of 400 to 4000  $\text{cm}^{-1}$  to observe chemical conformation of the functional groups in  $\text{TiO}_2$  at different calcination temperatures, as shown in Fig. 4. All spectra showed typical bands and signals for  $\text{TiO}_2$  (Sienkiewicz et al., 2021). A broad band in the region of 3660–2990  $\text{cm}^{-1}$  is attributed to stretching vibrations of the hydroxyl alcohol group (O–H), due to interaction with the hydroxyl group (OH) of the water molecule ( $\text{H}_2\text{O}$ ) (Sienkiewicz et al., 2021; Winter et al., 2009), which was confirmed by the presence of a weak band around 1637  $\text{cm}^{-1}$  (Senthilkumar et al., 2017). The bands recorded at 3130 and 3220  $\text{cm}^{-1}$  are indicative of the presence of OH groups on the  $\text{TiO}_2$  surface (Fernández-Catalá et al., 2017). This absorption band at 1637  $\text{cm}^{-1}$  refers to the bond Ti–OH and in addition, it is related to the coordinate vibration of bending of  $\text{H}_2\text{O}$  (Senthilkumar et al., 2017). The band observed in the range between 550 and 750  $\text{cm}^{-1}$  is related to the bending of the Ti–O and O–Ti–O bond. The location of the Ti–O vibrational mode varied from one phase to another, as it is located at 531, 566, and 509  $\text{cm}^{-1}$  for the  $\text{TiO}_2$ -rutile,  $\text{TiO}_2$ -anatase, and  $\text{TiO}_2$ -mixed phase, respectively. These results confirm that the calcination temperature increases gradually the crystalline nature of  $\text{TiO}_2$ . This can be observed by the behavior in the reduction of the O–H bond with the increase of the calcination temperature, and simultaneously with the intensity of the enhanced

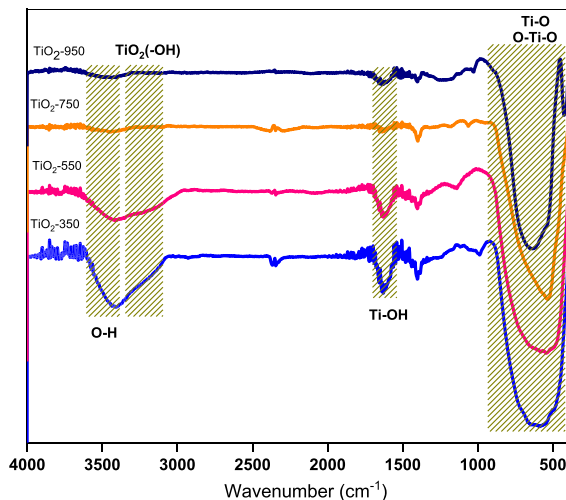


**Fig. 4** FT-IR spectra for TiO<sub>2</sub>-350, TiO<sub>2</sub>-550, TiO<sub>2</sub>-750 e TiO<sub>2</sub>-950

functional binding Ti–O and O–Ti–O (Senthilkumar et al., 2017).

### 3.2 Photocatalytic Studies

The photocatalytic activity of TiO<sub>2</sub> for different calcination temperatures was studied by performing the photodegradation of rhodamine B (RhB) and the photocatalytic conversion of glycerol.

#### 3.2.1 Photodegradation of RhB

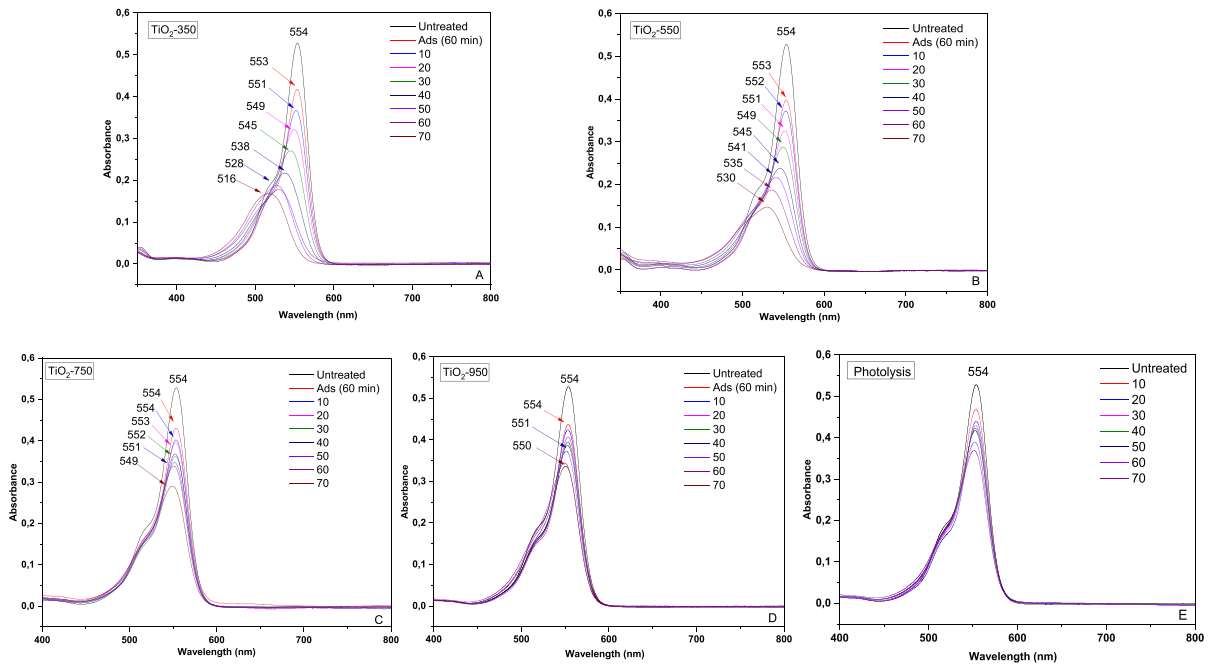
To evaluate TiO<sub>2</sub> at various temperatures and for use in environmental remediation, photodegradation of RhB was investigated as a model reaction. Changes in the UV–vis absorption spectra as a function of time and appropriate concentrations were then monitored to track the evolution of RhB degradation products. Thus, a total reaction period of 130 min was used to study the photodegradation of RhB, with 60 min used for adsorption (in the dark) and 70 min used for reaction while being exposed to UV-A light.

Figure 5 shows how the UV–vis absorption spectra changed as RhB underwent photodegradation. RhB maximum absorbance band is at 554 nm, and a decline in strength in this band maximum absorbance band suggests that this dye was gradually photodegraded by UV exposure.

As can be seen, for TiO<sub>2</sub>-350 (Fig. 5.a) RhB characteristic absorption band rapidly decreased along with a hypsochromic shift in the maximum absorption wavelength from 554 to 516 nm. Similar alterations have also been documented in earlier experiments utilizing photocatalysts TiO<sub>2</sub>/Bi<sub>2</sub>O<sub>3</sub> (Sharma et al., 2022), SnO<sub>2</sub> (De Assis et al., 2018). The sharp decrease in maximum absorption results from chromophore cleavage, while the peak shift is related to an N-deethylation mechanism, and RhB is completely N-deethylated when the absorption maximum shift moves from 554 to 498 nm (Watanabe et al., 1977; Zhuang et al., 2010) accompanied by the formation of a series of N-deethylated intermediates. It is also known that these reaction mechanisms can occur simultaneously (Watanabe et al., 1977; Zhuang et al., 2010) Thus, it was concluded that for TiO<sub>2</sub>-350 the cleavage of the chromophore from RhB occurs in this case, however, it is not the predominant mechanism. It can be seen from Fig. 5.a, that the maximum wavelength shift occurs faster than the complete decrease in main band absorbance at 554 nm. This behavior clearly indicates that the N-deethylation mechanism predominates in chromophore cleavage when using TiO<sub>2</sub>-350 as photocatalyst indicating that N-deethylation is easier than the cleavage of the entire conjugated chromophore structure of RhB in this reaction system, which is due to the fact that cleavage of the C–C bond requires more energy than the C–C bond N–C (Luo et al., 2020). For TiO<sub>2</sub>-550, it was observed that the hypsochromic shift was slightly interrupted, and chromophore cleavage was favored, Fig. 5.b. As the calcination temperature increased, as observed for TiO<sub>2</sub>-550 and TiO<sub>2</sub>-950, Fig. 5.c and 5.d, both mechanisms were negatively affected, with a considerable decrease in the photodegradation mechanism of RhB.

It is known that the efficiency of the photocatalyst is induced by isolated or combined properties, depending on the reaction mechanism. As observed, TiO<sub>2</sub>-350 presented a larger surface area (109.0 m<sup>2</sup>/g), and signs referring to the anatase phase of TiO<sub>2</sub> were identified, observing a marked hypsochromic shift. As the calcination temperature increased, there was a decrease surface area, and a transformation from the anatase to the rutile phase of TiO<sub>2</sub>, directly influencing the efficiency. It is possible to observe that according to the XRD and Raman, the anatase phase was identified with greater clarity for





**Fig. 5** Spectral changes showing RhB photodegradation achieved with the catalysts (A)  $\text{TiO}_2$ -350 (B)  $\text{TiO}_2$ -550; (C)  $\text{TiO}_2$ -750 (D)  $\text{TiO}_2$ -950 (E) photolysis

$\text{TiO}_2$ -550 ( $69.0 \text{ m}^2/\text{g}$ ), however, it presented a smaller surface area compared to  $\text{TiO}_2$ -350. Thus, it can be inferred that the material with the highest surface area influenced the n-deethylation mechanism, but the anatase phase was responsible for the greater cleavage of the chromophore. For  $\text{TiO}_2$ -750 ( $9.0 \text{ m}^2/\text{g}$ ), where the beginning of the transformation from the anatase phase to the rutile phase of  $\text{TiO}_2$  was observed, both mechanisms were markedly affected, as well as for  $\text{TiO}_2$ -950, composed of the rutile phase of  $\text{TiO}_2$ . It is important to mention that the higher surface area of  $\text{TiO}_2$ -350, and possibly the higher amorphous phase content, plays an essential role in the presence of OH groups on the surface (Dlamini et al., 2022). Not always a larger surface area will have a good quality of site distribution, but in this case, the potential role of the amorphous phase of  $\text{TiO}_2$ , and a larger surface area seems to have affected the photocatalytic efficiency, and consequently improved the photodegradation mechanisms of RhB. This can be confirmed by the behavior in the reduction of the O–H bond with the increase of the calcination temperature, according to the FTIR results shown in Fig. 4. It is assumed that the  $\bullet\text{OH}$  radicals yielded on the surface readily attack the diethylamino groups efficiently (Zhuang

et al., 2010), resulting in the N-deethylation of RhB molecules in the presence of photocatalysts of greater surface area.

Regarding the intermediate products from the photodegradation of RhB, in the current investigation the complete deethylation of the RhB dye (hypsochromic shift from 554 to 498 nm) was not observed, but in 70 min of reaction for  $\text{TiO}_2$ -350 and  $\text{TiO}_2$ -550 it was possible to observe the displacement of this same band, in addition to the decrease in the main band, showing three N-de-ethylations, and formation of three co-products: N,N,N'-Triethyl-rhodamine (539 nm), N,N'-Diethyl-rhodamine (522 nm), N'-Ethyl-rhodamine (510 nm) (Pica et al., 2018; Khanam & Rout, 2022). In relation to  $\text{TiO}_2$ -750 and  $\text{TiO}_2$ -950, only the breakage of the chromophore groups is observed, as evidenced by the decrease in absorbance as a function of time. In both reactions from 40 min onward it is possible to identify a slight shift of the signals, but it was not possible to confirm the formation of by-products for the reactions using  $\text{TiO}_2$ -750 and  $\text{TiO}_2$ -950. Still, on the by-products determined in the present study it is important to emphasize that in previous studies a low degree of toxicity of the products generated from the

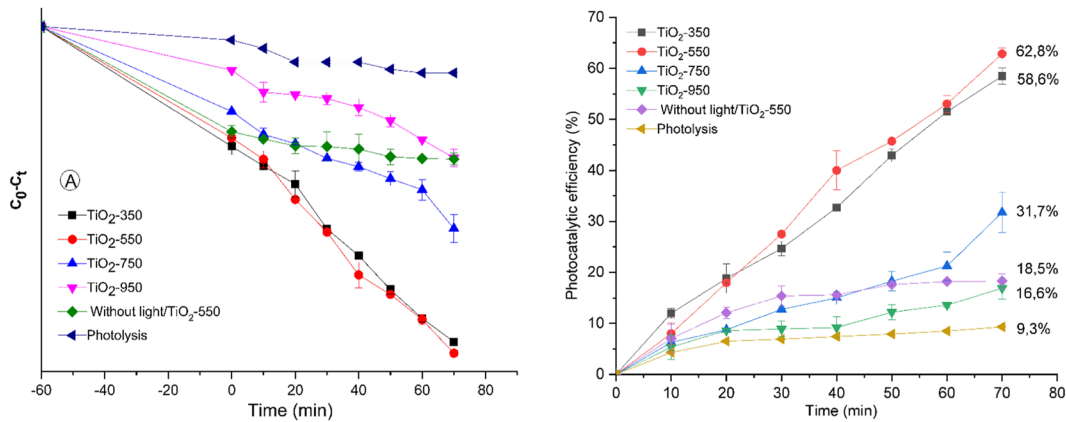


**Fig. 6** **A**) Plot of  $\ln(C/C_0)$  vs. irradiation time for photocatalytic degradation of RhB and **B**) percentage degradation of RhB using TiO<sub>2</sub>-350; TiO<sub>2</sub>-550; TiO<sub>2</sub>-750; TiO<sub>2</sub>-950; photolysis and without light/with catalyst

n-deethylation of RhB has already been demonstrated (Zhang et al., 2022).

To confirm that the photocatalytic activity is due to the photocatalyst only, we performed blank experiments without catalyst under light (photolysis), as shown in Fig. 5.e. It was noted that 13% of RhB was degraded after 70 min. The ability of the RhB dye to absorb UV light, which is sufficient to break the bonds in the chromophore groups, is one reason for this phenomenon. However, photolysis only makes up a minor portion of the photodegradation process and does not result in a rapid or thorough breakdown. These observations are confirmed by the results obtained for the photodegradation of the RhB dye as a function of time (see Fig. 6.a), calculated in relation to its maximum absorbance (554 nm), in the presence of the photocatalysts under study (TiO<sub>2</sub>-350, TiO<sub>2</sub>-550, TiO<sub>2</sub>-750 and TiO<sub>2</sub>-950) and without a catalyst. Figure 6.b shows the percentages obtained in the photodegradation of RhB.

In fact, previous studies have shown that TiO<sub>2</sub> phase transformation resulting from an increase in calcination temperature can cause changes in surface, structural and optical properties (Cai et al., 2016; Pelaez et al., 2010). The increase in TiO<sub>2</sub> calcination resulted in an increase in crystallite size, and consequently an abrupt decrease in surface area. Knowing that photocatalysis is a combination of reactional factors, in the present case, it seems that the surface area was a determining factor for the photocatalytic efficiency.

In this study, for the TiO<sub>2</sub> catalysts calcined at different temperatures, it was found that the photocatalytic activity decreased, as mentioned above. Thus, the best performance in terms of photocatalytic activity was obtained with TiO<sub>2</sub>-550, with a maximum degradation value of 62.8% after 70 min, compared with 60.7, 26.4 and 23.4% for TiO<sub>2</sub>-350, TiO<sub>2</sub>-750, and TiO<sub>2</sub>-950, respectively (see Fig. 6b).

The results reported here demonstrate that it is possible to synthesize TiO<sub>2</sub> by modulating the calcination temperature and obtain photocatalysts that can be used with visible light (for example, sunlight) for photocatalytic purposes, taking advantage of the attractive properties of TiO<sub>2</sub>, such as nontoxic, high environmental stability and sustainability. This observation is based on the band gap decrease, as the calcination temperature increases, for TiO<sub>2</sub>-350, TiO<sub>2</sub>-550, TiO<sub>2</sub>-750 and TiO<sub>2</sub>-950, the band gap values obtained were 3.0, 2.9, 2.8, and 2.7 eV, respectively.

The photocatalytic degradation of RhB has been considered by previous reports as a first-order reaction, and the rate constant can be determined according to Eq. 6, considering that  $t$  is the reaction time,  $C_0$  and  $C_t$  are the RhB concentrations at initial and reaction time  $t$ , respectively (Cheng et al., 2017; Zhang et al., 2020).

$$C = C_0 e^{-kt} \quad (6)$$

For TiO<sub>2</sub> calcined at different temperatures, Fig. 7 shows reaction rate constant  $k$ . In addition, to examining the photocatalytic efficiency by decreasing the

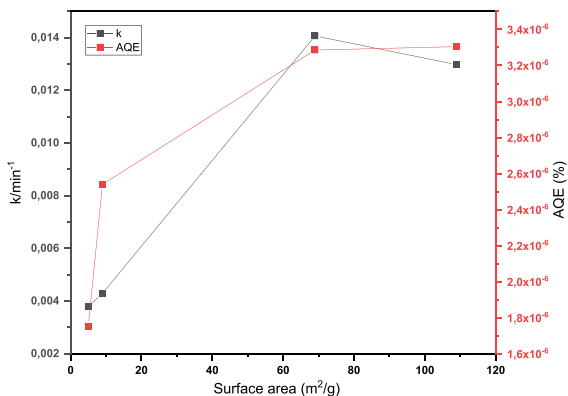


**Fig. 7** Photocatalytic reaction rate constant of RhB and apparent quantum efficiencies of the TiO<sub>2</sub> calcined at different temperatures with different surface areas

concentration of RhB, in the reaction medium, it is important to estimate the Apparent Quantum Efficiency (AQE) of the investigated photocatalysts (Eq. 7), which can be calculated by Eq. 8 ( $d[x]/dt$  is the initial rate of change of the concentration of the reactant and  $d[h\nu]_{inc}/dt$  is the total optical power (TOP) impinging on the sample) (Bahruji et al., 2019).

$$AQE \Phi = \frac{\text{Number of molecules converted}}{\text{Total photons absorbed}} \quad (7)$$

$$AQE = \frac{d[x]/dt}{d[h\nu]_{inc}/dt} = \frac{kC_0}{TOP} \quad (8)$$

For the degradation of RhB, in the present investigation  $d[x]/dt = kC_0$ . Moreover, as photocatalysts had different surface areas, a relationship was established between the amount of the photocatalyst used (0.3 g/L) and the surface area of the different photocatalysts (being 109.0; 69.0; 9.0 and 5.0 m<sup>2</sup>/g, for TiO<sub>2</sub>-350; TiO<sub>2</sub>-550; TiO<sub>2</sub>-750; TiO<sub>2</sub>-950, respectively). The optical power incident on the suspension was 5 mW mL<sup>-1</sup>. As previously presented, Fig. 7 shows that the apparent quantum efficiency of the reaction was affected by the surface area, as well as k, showing that photocatalysts with larger surface area were favoured with the activation of sites on the surface by means of incident photons. In view of this, it is important to understand that although the presence of photons is essential to drive the photocatalytic reaction, the ability of the photocatalyst to absorb

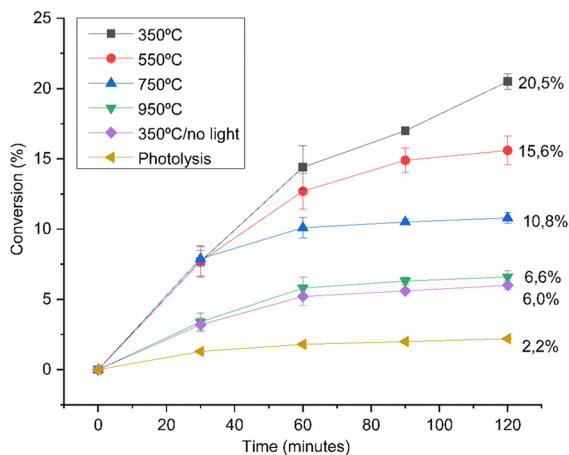


**Fig. 8** Conversion of glycerol to TiO<sub>2</sub> calcined at different temperatures, with catalyst TiO<sub>2</sub>-350/without light and photolysis

photons is also important to increase the reactivity (Cheng et al., 2017).

### 3.2.2 Photocatalytic Conversion of Glycerol

The photocatalytic activity of TiO<sub>2</sub> obtained at different calcination temperatures was also investigated in the photocatalytic conversion of glycerol, 2 h of lighting.

Figure 8 shows the results of photocatalytic conversion of glycerol as a function of time. No significant conversion was found under photolysis (2.2%). The use of TiO<sub>2</sub>-350 led to a conversion of 20.5% of glycerol, followed by TiO<sub>2</sub>-550, TiO<sub>2</sub>-750, TiO<sub>2</sub>-950, with 15.6%, 10.8%, 6.6%, respectively. Such behavior suggests a strong influence of the combination of structural, surface and electronic properties. We can observe an influence of the surface area of the photocatalysts, which was directly affected by the calcination temperature. The TiO<sub>2</sub>-350 photocatalyst showed a greater surface area, reaching 109.0 m<sup>2</sup>/g, and this greater surface area may have favored a better use of the emitted photons, promoting an effective separation of charge carriers. Furthermore, a larger surface area may suggest the presence of more active sites available for water molecules to be adsorbed on the TiO<sub>2</sub> surface and the formation of reactive species occurs. Furthermore, the adsorption of substrate molecules

directly on the catalyst surface can be favored in materials with high surface area (Saif et al., 2010), and in this case, the hole generated in the photoactivation of the semiconductor can directly promote the glycerol oxidation reaction.

Regarding the crystalline phases of  $\text{TiO}_2$ -350 and  $\text{TiO}_2$ -550, they are mostly present in the anatase crystalline form, and even though the same crystalline phase is observed in both materials, due to the different calcination temperatures the materials have different electronic and surface properties, as already mentioned. Evaluating the activity of  $\text{TiO}_2$ -550 in the conversion of glycerol, it is possible to see that the photocatalytic activity of the material is closely related to its structural and surface properties, because, even with a smaller surface area compared to  $\text{TiO}_2$ -350, the use of  $\text{TiO}_2$ -550 led to 15.6% glycerol conversion. In addition to the surface area, this can be attributed to the combination of the anatase and rutile phase of  $\text{TiO}_2$ -550, as observed in the Raman measurements, which may have facilitated the promotion of electrons between the energy bands of the semiconductor. In the present study it was observed that the mixed phase  $\text{TiO}_2$ -550 photocatalyst containing both anatase and rutile expressed higher photocatalytic activity than pure rutile. It is important to mention that this phenomenon of a synergistic effect between the anatase and rutile phase in relation to photocatalytic activity has already been observed previously, as discussed by Zerjav et al. (2022).

Still, the observations reported here corroborate recent studies, since according to Zerjav et al. (2022)

when the mixture of anatase and rutile is used as a photocatalyst, the anatase part represents the main booster phase responsible for the higher concentration of  $\text{OH}^\cdot$  radicals in the reaction system. However, in a mixed phase system, the anatase phase could not generate the same amount of  $\text{OH}^\cdot$  radicals in the mixture, compared to when only the anatase phase was investigated, due to the “shading” effect caused by small and abundant rutile particles. Furthermore, the rutile particles were acting as a UV light filter for the anatase particles as they are able to collect UV light over a wider range (Zerjav et al. (2022)). For this reason, in the current investigation,  $\text{TiO}_2$ -350 (anatase phase) exhibits the highest photocatalytic activity.

Figure 9 shows the main oxidation products observed from the photocatalytic conversion of glycerol, which were glyceraldehyde, glycolic and tartronic acid, and the selectivity was highly influenced by the nature of the photocatalyst as shown in Fig. 9a and b.

Starting with the most active photocatalyst,  $\text{TiO}_2$ -350, predominantly composed of the anatase phase, we can clearly observe that the main oxidation products, such as glycolic acid and glyceraldehyde, are produced in a short reaction period of 30 min, and the selectivity did not vary according to time increased; a similar result was observed for  $\text{TiO}_2$ -550. In the case of the  $\text{TiO}_2$ -750 and  $\text{TiO}_2$ -950 (rutile) photocatalyst, although the distribution and amount of products were different, as expected in view of the lower overall conversion observed, seemed to be selective to glycolic acid, proving that the crystalline

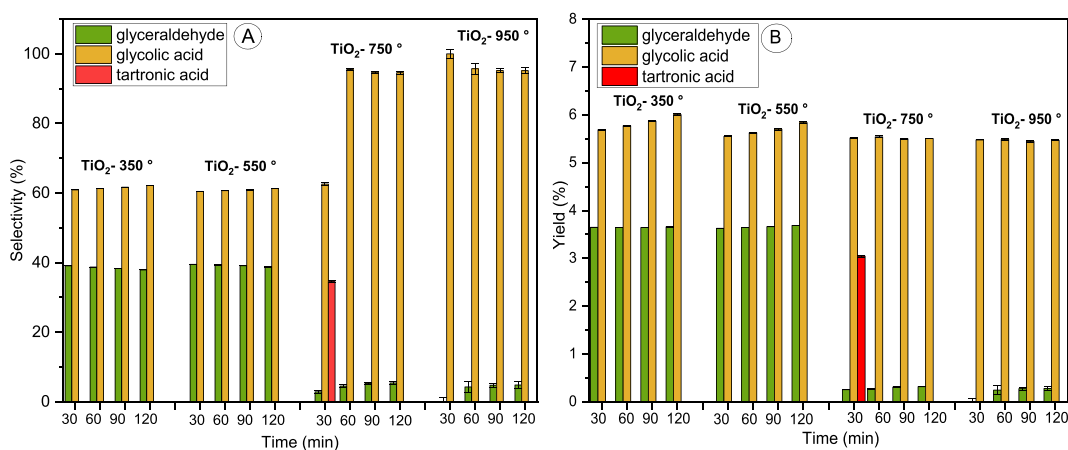


**Fig. 9** (A) Variation in selectivity and (B) variation in yield, based on glycerol conversion

phase influenced the distribution of the products formed.

Initially, the main products detected were glycolic acid and glyceraldehyde, and smaller amounts of other oxidized products, such as tartronic acid. These results suggest that in the first step of the reaction mechanism, glycerol undergoes the first oxidation towards glyceraldehyde, as observed in Wang et al. (2019). Considering that glyceraldehyde is a result of the oxidation of primary (terminal) OH groups of glycerol and that we have two primary OH groups, the probability of being produced is much higher compared to the production of dihydroxyacetone, which is a result of the oxidation of the secondary OH group in the glycerol, as mentioned by Yu et al. (2021). The glycerol conversion increased with the reaction time, as shown in Fig. 8, but the selectivity for glyceraldehyde decreased, and the main product was glycolic acid (Wang et al., 2019). Glyceraldehyde, in turn, can also be oxidized to glycolic acid. Another possible route of glycolic acid formation occurs through the cleavage of the C1-C2 carbons of glycerol (Cai et al., 2014; Choi et al., 2020). For TiO<sub>2</sub>-750, the selectivity of 34.5% of tartronic acid was identified, and this effect can be explained by parallel reactions in which two hydroxyl radicals, formed from the photocatalytic process, react simultaneously with the C1 and C3 carbons of the glycerol, converting it directly to tartronic acid in a single step (Cai et al., 2014).

#### 4 Conclusions

The results indicate that the calcination temperature can significantly affect the physical properties of TiO<sub>2</sub> powders. As the calcination temperature increased, the rate of RhB degradation decreased. It was observed that TiO<sub>2</sub>-350 and TiO<sub>2</sub>-550 presented similar photocatalytic efficiency rates of 60.7 and 62.8%, respectively. For TiO<sub>2</sub>-750 and TiO<sub>2</sub>-950 the efficiency decreased significantly, to 26.4 and 23.7%, respectively. Despite the literature has already reported that the rutile phase of TiO<sub>2</sub> has the lowest photocatalytic activity, due to the lower number of active sites and hydroxyl groups on the surface (Sienkiewicz et al., 2021), here we show that combination it was observed that the combination of anatase–rutile phases can favor the increase of photocatalytic efficiency. The decrease in photocatalytic activity with

increasing calcination temperature may be related to a number of factors. First, corroborating the results of XRD and Raman, the phase transformation of anatase to rutile started at 550 °C. Another important factor to be highlighted is that the sintering and growth of TiO<sub>2</sub> crystallites result in a significant decrease in the TiO<sub>2</sub> surface area. Although RhB is frequently investigated in heterogeneous photocatalysis, herein we show that their degradation actually occurs, and it was estimated by the identification of less toxic by-products (Zhang et al., 2022), formed by process of n-deethylation. For the glycerol photocatalytic conversion system, evaluating the results obtained from conversion, selectivity, and yield in the photocatalytic tests, it is possible to observe that the surface, electronic and structural properties strongly influence the direction of the photocatalytic reactions. The use of materials calcined at temperatures of 350 and 550°C led to a greater conversion of glycerol, but the selectivity and yield results show that catalysts calcined at higher temperatures (750 and 950°C) have greater selectivity, that is, the transformation of crystalline phases anatase to rutile directed the selectivity of the reaction to glycolic acid. This result is promising for future applications, since glycolic acid is a molecule widely applied on an industrial scale in several industrial sectors (Choi et al., 2020). The results showed that the increase in the calcination temperature had a strong influence on the glycerol conversion and on the selectivity of the products formed, which may be interesting for practical applications, since the preferential formation of certain products can contribute to more efficient routes to produce them.

**Acknowledgements** This research was supported by the National Council for Scientific and Technological Development (CNPq), the Brazilian Federal Agency for the Improvement of Higher Education (CAPES), the Brazilian Innovation Agency (FINEP) and the Alagoas Research Foundation (FAPEAL). GCA and IMAS express their appreciation for fellowships granted by CAPES and CNPq. MRM and SMPM thank CNPq for research fellowships. The authors also thank the LSCAT-CTEC team for their contributions.

**Author Contribution** Igor Mateus de Amorim Silva conceived and designed the experiments, methodology, experimental work, data collection and analysis, performed experiments, data collection and analysis and reviewed draft versions of the manuscript;

Geovânia Cordeiro de Assis conceived and designed the experiments, methodology, experimental work, data collection and analysis, performed experiments, data collection and

analysis and reviewed draft versions of the manuscript; Cristian José Giertyas conceived and designed the methodology, data analysis, performed experiments, and reviewed draft versions of the manuscript; Janaína Heberle Bortoluzzi conceived and designed the methodology, data analysis, performed experiments, and reviewed draft versions of the manuscript; Tiago Gomes dos Santos conceived and designed the methodology, data analysis, performed experiments, and reviewed draft versions of the manuscript; Mario Roberto Meneghetti conceived and designed the experiments, research methodology, supervised the research, evaluated data and interpretation, drafted, reviewed and edited the manuscript, administered the project and acquired the research funding; Simoni Margareti Plentz Meneghetti conceived and designed the experiments, research methodology, supervised the research, evaluated data and interpretation, drafted, reviewed and edited the manuscript, administered the project and acquired the research funding.

**Funding** This research was supported by the National Council for Scientific and Technological Development (CNPq), the Brazilian Federal Agency for the Improvement of Higher Education (CAPES), the Brazilian Innovation Agency (FINEP) and the Alagoas Research Foundation (FAPEAL). GCA and IMAS express their appreciation for fellowships granted by CAPES and CNPq. MRM and SMPM thank CNPq for research fellowships.

**Data Availability** The authors declare that the data supporting the findings of this study are available within the paper.

**Code Availability** Not applicable.

**Declarations**

**Ethics Approval** Not applicable.

**Consent to Participate** Not applicable.

**Consent for Publication** Not applicable.

**Conflict of Interest** The authors declare no competing interests.

## References

- Abdullah, F. H., Abu Bakar, N. H. H., & Abu Bakar, M. (2022). Current advancements on the fabrication, modification, and industrial application of zinc oxide as photocatalyst in the removal of organic and inorganic contaminants in aquatic systems. *Journal of Hazardous Materials*, *424*, 127416. <https://doi.org/10.1016/j.jhazmat.2021.127416>
- Aihemaiti, X., Wang, X., Li, Y., Wang, Y., Xiao, L., Ma, Y., Qi, K., Zhang, Y., Liu, J., & Li, J. (2022). Enhanced photocatalytic and antibacterial activities of S-scheme SnO<sub>2</sub>/Red phosphorus photocatalyst under visible light. *Chemosphere*, *296*, 134013. <https://doi.org/10.1016/j.chemosphere.2022.134013>
- Araujo, R. N., Nascimento, E. P., Firmino, H. C. T., Macedo, D. A., Neves, G. A., Morales, M. A., & Menezes, R. R. (2021).  $\alpha$ -Fe<sub>2</sub>O<sub>3</sub> fibers: An efficient photocatalyst for dye degradation under visible light. *Journal of Alloys and Compounds*, *882*, 160683. <https://doi.org/10.1016/j.jallcom.2021.160683>
- Arfaoui, A., Mhamdi, A., Besrou, N., Touihri, S., Ouzari, H. I., Alrowaili, Z. A., & Amlouk, M. (2018). Investigations into the physical properties of SnO<sub>2</sub>/MoO<sub>3</sub> and SnO<sub>2</sub>/WO<sub>3</sub> bi-layered structures along with photocatalytic and antibacterial applications. *Thin Solid Films*, *648*, 12–20. <https://doi.org/10.1016/j.tsf.2018.01.002>
- Bahruji, H., Maarof, H., & Abdul Rahman, N. (2019). Quantum efficiency of Pd/TiO<sub>2</sub> catalyst for photocatalytic reforming of methanol in ultra violet region. *Chemical Papers*, *73*, 2707–2714. <https://doi.org/10.1007/s11696-019-00822-w>
- Bera, D., Qian, L., Tseng, T.-K., & Holloway, P. H. (2010). Quantum Dots and Their Multimodal Applications: A Review. *Materials*, *3*, 2260–2345. <https://doi.org/10.3390/ma3042260>
- Bodke, M. R., Purushotham, Y., & Dole, B. N. (2018). Comparative study on zinc oxide nanocrystals synthesized by two precipitation methods. *Cerâmica*, *64*, 91–96. <https://doi.org/10.1590/0366-69132018643692207>
- Buraso, W., Lachom, V., Siriya, P., & Laokul, P. (2018). Synthesis of TiO<sub>2</sub> nanoparticles via a simple precipitation method and photocatalytic performance. *Materials Research Express*, *05*, 115003. <https://doi.org/10.1088/2053-1591/aadbf0>
- Byrne, C., Fagan, R., Hinder, S., McCormack, D. E., & Pillai, S. C. (2016). New approach of modifying the anatase to rutile transition temperature in TiO<sub>2</sub> photocatalysts. *RSC Advances*, *6*, 95232–95238. <https://doi.org/10.1039/C6RA19759K>
- Cai, J., Ma, H., Zhang, J., Du, Z., Huang, Y., Gao, J., & Xu, J. (2014). Catalytic oxidation of glycerol to tartronic acid over Au/HY catalyst under mild conditions. *Chinese Journal of Catalysis*, *35*, 1653–1660. [https://doi.org/10.1016/S1872-2067\(14\)60132-7](https://doi.org/10.1016/S1872-2067(14)60132-7)
- Cai, J., Xin, W., Liu, G., Lin, D., & Zhu, D. (2016). Effect of calcination temperature on structural properties and photocatalytic activity of Mn-C-codoped TiO<sub>2</sub>. *Materials Research*, *19*, 401–407. <https://doi.org/10.1590/1980-5373-MR-2015-0381>
- Cassaignon, S., Koelsch, M., & Jolivet, J.-P. (2007). From TiCl<sub>3</sub> to TiO<sub>2</sub> nanoparticles (anatase, brookite and rutile): Thermohydrolysis and oxidation in aqueous medium. *Journal of Physics and Chemistry of Solids*, *68*, 695–700. <https://doi.org/10.1016/j.jpics.2007.02.020>
- Çetinkaya, S., Khamidov, G., Ozcan, L., Palmisano, L., & Yurdakal, S. (2022). Selective photoelectrocatalytic oxidation of glycerol by nanotube, nanobelt and nanosponge structured TiO<sub>2</sub> on Ti plates. *Journal of Environmental Chemical Engineering*, *10*, 107210. <https://doi.org/10.1016/j.jece.2022.107210>
- Chauhan, P. S., Kumar, K., Singh, K., & Bhattacharya, (2022). Fast decolorization of rhodamine-B dye using novel

- V<sub>2</sub>O<sub>5</sub>-rGO photocatalyst under solar irradiation. *Synthetic Metals*, 283, 116981. <https://doi.org/10.1016/j.synthmet.2021.116981>
- Cheng, J., Wang, Y., Xing, Y., Shahid, M., & Pan, W. (2017). A stable and highly efficient visible-light photocatalyst of TiO<sub>2</sub> and heterogeneous carbon core-shell nanofibers. *RSC Advances*, 25, 15330–15336. <https://doi.org/10.1039/C7RA00546F>
- Choi, Y., Nunotani, N., & Imanaka, N. (2020). Glyceraldehyde production from glycerol over Pt/CeO<sub>2</sub>-ZrO<sub>2</sub>-Fe<sub>2</sub>O<sub>3</sub>/SBA-16 catalysts around room temperature in open air system. *Materials Letters*, 283, 128–392. <https://doi.org/10.1016/j.matlet.2020.128392>
- Choudhury, B., & Choudhury, A. (2013). Local structure modification and phase transformation of TiO<sub>2</sub> nanoparticles initiated by oxygen defects, grain size, and annealing temperature. *Int. Nano Lett*, 3, 55. <https://doi.org/10.1186/2228-5326-3-55>
- De Assis, G. C., Skovroinski, E., Leite, V. D., Rodrigues, M. O., Galembek, A., Alves, M. C. F., Eastoe, J., & De Oliveira, R. J. (2018). Conversion of “Waste Plastic” into Photocatalytic Nanofoams for Environmental Remediation. *ACS Applied Materials & Interfaces*, 10, 8077–8085. <https://doi.org/10.1021/acsami.7b19834>
- Dlamini, M. C., Dlamini, M. L., Mente, P., Tlhaole, B., Erasmus, R., Maubane-Nkadingeng, M. S., & Moma, J. A. (2022). Photocatalytic abatement of phenol on amorphous TiO<sub>2</sub>-BiOBr-bentonite heterostructures under visible light irradiation. *Journal of Industrial and Engineering Chemistry*, 111, 419–436. <https://doi.org/10.1016/j.jiec.2022.04.023>
- Domínguez-Jaimes, L. P., Cedillo-González, E. I., Luévano-Hipólito, E., Acuña-Bedoya, J. D., & Hernández-López, J. M. (2021). Degradation of primary nanoplastics by photocatalysis using different anodized TiO<sub>2</sub> structures. *Journal of Hazardous Materials*, 413, 125452. <https://doi.org/10.1016/j.jhazmat.2021.125452>
- Fathi-Hafshejani, P., Johnson, H., Ahmadi, Z., Roach, M., Shamsaei, N., & Mahjouri-Samani, M. (2020). Phase-Selective and Localized TiO<sub>2</sub> Coating on Additive and Wrought Titanium by a Direct Laser Surface Modification Approach. *ACS Omega*, 27, 16744–16751. <https://doi.org/10.1021/acsomega.0c01671>
- Fernández-Catalá, J., Cano-Casanova, L., Lillo-Ródenas, M. A., Berenguer-Murcia, M., & Cazorla-Amorós, D. (2017). Synthesis of TiO<sub>2</sub> with Hierarchical Porosity for the Photooxidation of Propene. *Molecules*, 22, 2243. <https://doi.org/10.3390/molecules22122243>
- Franco, M., Marin, O., Vega, N. C., Tirado, M., Tereschuk, M. L., & Comendi, D. (2022). Surface nanostructuring of ZnO and ZnO: Cd sub-microstructures and their use as suspended and immobilized photocatalysts for rapid degradation of methylene blue. *Materials Letters*, 311, 131634. <https://doi.org/10.1016/j.matlet.2021.131634>
- Gao, Y., Wang, H., Wu, J., Zhao, R., Lu, Y., & Xin, B. (2014). Controlled facile synthesis and photocatalytic activity of ultrafine high crystallinity TiO<sub>2</sub> nanocrystals with tunable anatase/rutile ratios. *Applied Surface Science*, 294, 36–41. <https://doi.org/10.1016/j.apsusc.2013.12.107>
- Geetha, N., Sivaranjani, S., Ayeshamariam, A., Siva, B. M., Nivetha, S., Kaviyarasu, N., & Jayachandran, M. (2018). High Performance Photo-Catalyst Based on Nanosized ZnO–TiO<sub>2</sub> Nanoplatelets for Removal of RhB Under Visible Light Irradiation. *Journal of Advanced Microscopy Research*, 13, 12–19. <https://doi.org/10.1166/jamr.2018.1352>
- Giraldo-Aguirre, A. L., Erazo-Erazo, E. D., Flórez-Acosta, O. A., Serna-Galvis, E. A., & Torres-Palma, R. A. (2015). TiO<sub>2</sub> photocatalysis applied to the degradation and antimicrobial activity removal of oxacillin: Evaluation of matrix components, experimental parameters, degradation pathways and identification of organics by-products. *Journal of Photochemistry and Photobiology a: Chemistry*, 311, 95–103. <https://doi.org/10.1016/j.jphotochem.2015.06.021>
- Gonciarz, A., Pich, R., Bogdanowicz, K. A., Drabczyk, K., Sypien, A., Major, Ł., & Iwan, A. (2021). TiO<sub>2</sub> and TiO<sub>2</sub>-Ag powders and thin layer toward self-cleaning coatings for PV panel integrated with sound-absorbing screens: Technical approaches. *Journal of Power Sources*, 8, 100053. <https://doi.org/10.1016/j.powera.2021.100053>
- He, J., Du, Y., Bai, Y., An, J., Cai, X., Chen, Y., Wang, P., Yang, X., & Feng, Q. F. (2019). Facile Formation of Anatase/Rutile TiO<sub>2</sub> Nanocomposites with Enhanced Photocatalytic Activity. *Molecules*, 24, 2996. <https://doi.org/10.3390/molecules24162996>
- Helmiyati, H., Fitriana, N., Chaerani, M. L., & Dine, F. W. (2022). Green hybrid photocatalyst containing cellulose and γ-Fe<sub>2</sub>O<sub>3</sub>-ZrO<sub>2</sub> heterojunction for improved visible-light driven degradation of Congo red. *Optical Materials*, 124, 111982. <https://doi.org/10.1016/j.optmat.2022.111982>
- Hojamberdiev, M., Czech, B., Göktaş, A. C., Yubuta, K., & Kadirova, Z. C. (2020). SnO<sub>2</sub>@ZnS photocatalyst with enhanced photocatalytic activity for the degradation of selected pharmaceuticals and personal care products in model wastewater. *Journal of Alloys and Compounds*, 827, 154339. <https://doi.org/10.1016/j.jallcom.2020.154339>
- Hu, J., Zhang, S., Cao, Y., Wang, H., Yu, H., & Peng, F. (2018). Novel Highly Active Anatase/Rutile TiO<sub>2</sub> Photocatalyst with Hydrogenated Heterophase Interface Structures for Photoelectrochemical Water Splitting into Hydrogen. *ACS Sustainable Chemistry & Engineering*, 6, 10823–10832. <https://doi.org/10.1021/acssuschemeng.8b02130>
- Hu, J., Zhao, R., Li, H., Xu, Z., Dai, H., Gao, H., Yu, H., Wang, Z., Wang, Y., Liu, Y., Han, J., & Guo, R. (2022). Boosting visible light photocatalysis in an Au@TiO<sub>2</sub> yolk-in-shell nanohybrid. *Applied Catalysis. B*, 303, 120869. <https://doi.org/10.1016/j.apcatb.2021.120869>
- Imbault, A. L., & Farnood, R. (2020). Selective Oxidation of Crude Glycerol to Dihydroxyacetone in a Biphasic Photoreactor. *Catalysts*, 10, 360. <https://doi.org/10.3390/catal10040360>
- Iqbal, A., Ahmed, A. S., Ahmad, N., Shafi, A., Ahamad, T., Khan, M. Z., & Srivastava, S. (2021). Biogenic synthesis of CeO<sub>2</sub> nanoparticles and its potential application as an efficient photocatalyst for the degradation of toxic amido black dye. *Environmental Nanotechnology, Monitoring and Management*, 16, 100505. <https://doi.org/10.1016/j.enmm.2021.100505>

- Jedsukontorn, T., Saito, N., & Hunsom, M. (2018). Photoinduced Glycerol Oxidation over Plasmonic Au and AuM (M = Pt, Pd and Bi) Nanoparticle-Decorated TiO<sub>2</sub> Photocatalysts. *Journal of Nanomaterials*, 8, 269. <https://doi.org/10.3390/nano8040269>
- Jin, B., Yao, G., Wang, X., Ding, K., & Jin, F. (2017). Photocatalytic Oxidation of Glucose into Formate on Nano TiO<sub>2</sub> Catalyst. *ACS Sustainable Chemistry & Engineering*, 5, 6377–6381. <https://doi.org/10.1021/acssuschemeng.7b00364>
- Joseph, C. G., Taufiq-Yap, Y. H., Musta, B., Sarjadi, M. S., & Elilarasi, L. (2021). Application of Plasmonic Metal Nanoparticles in TiO<sub>2</sub>-SiO<sub>2</sub> Composite as an Efficient Solar-Activated Photocatalyst: A Review Paper. *Frontiers in Chemistry*, 08, 568063. <https://doi.org/10.3389/fchem.2020.568063>
- Kalaivani, T., & Anilkumar, P. (2017). Role of Temperature on the Phase Modification of TiO<sub>2</sub> Nanoparticles Synthesized by the Precipitation Method. *SILICON*, 10, 1679–1686. <https://doi.org/10.1007/s12633-017-9652-8>
- Kamarulzaman, N., Abdul Aziz, N. D., Kasim, M. F., & Chayed, N. F. (2019). Yahaya Subban, R. H., Badar, N. Anomalies in wide band gap SnO<sub>2</sub> nanostructures. *Journal of Solid State Chemistry*, 277, 271–280. <https://doi.org/10.1016/j.jssc.2019.05.035>
- Kar, A., Kundu, S., & Patra, A. (2010). Surface Defect-Related Luminescence Properties of SnO<sub>2</sub> Nanorods and Nanoparticles. *Journal of Physical Chemistry C*, 115, 118–124. <https://doi.org/10.1021/jp110313b>
- Khan, M. M. (2018). Metal oxide powder photocatalysts. In Z. Lin, M. Ye, & M. Wang (Eds.), *Multifunctional Photocatalytic Materials for Energy* (pp. 5–18). Woodhead Publishing in Materials.
- Khanam, S., & Rout, S. K. (2022). Enhanced Photocatalytic Oxidation of RhB and MB Using Plasmonic Performance of Ag Deposited on Bi<sub>2</sub>WO<sub>6</sub>. *Chemistry*, 4, 272–296. <https://doi.org/10.3390/chemistry4020022>
- Kim, M. G., Kang, J. M., Lee, J. E., Kim, K. S., Kim, K. H., Cho, M., & Lee, S. G. (2021). Effects of Calcination Temperature on the Phase Composition, Photocatalytic Degradation, and Virucidal Activities of TiO<sub>2</sub> Nanoparticles. *ACS Omega*, 6, 10668–10678. <https://doi.org/10.1021/acsomega.1c00043>
- Lal, M., Sharma, P., & Ram, C. (2021). Calcination temperature effect on titanium oxide (TiO<sub>2</sub>) nanoparticles synthesis. *Optik*, 241, 166934. <https://doi.org/10.1016/j.ijleo.2021.166934>
- Lazau, C., Poienar, M., Orha, C., Ursu, D., Nicolaescu, M., Vajda, M., & Bandas, C. (2021). Development of a new “n-p” heterojunction based on TiO<sub>2</sub> and CuMnO<sub>2</sub> synergy materials. *Materials Chemistry and Physics*, 272, 124999. <https://doi.org/10.1016/j.matchemphys.2021.124999>
- Lee, Y., Ahn, J. H., Shin, S., Jung, S.-H., Park, H.-S., Cho, Y.-G., Lee, D.-G., Kong, H., Lee, J. H., & Song, H.-K. (2022). Metal-nitrogen intimacy of the nitrogen-doped ruthenium oxide for facilitating electrochemical hydrogen production. *Applied Catalysis B: Environmental*, 303, 120873. <https://doi.org/10.1016/j.apcatb.2021.120873>
- Li, R., & Li, C. (2017). Chapter one-photocatalytic water splitting on semiconductor-based photocatalysts. In C. Song (Ed.), *Advances in catalysis* (pp. 1–57). Elsevier. <https://doi.org/10.1016/bs.acat.2017.09.001>
- Li, Q., Liu, Y., Wan, Z., Cao, H., Zhou, Y., Ye, X., Liu, X., & Zhang, D. (2021). Microwave-assisted synthesis of oxygen vacancy associated TiO<sub>2</sub> for efficient photocatalytic nitrate reduction. *Chinese Chemical Letters*, 33, 3835–3841. <https://doi.org/10.1016/j.ccllet.2021.12.025>
- Li, Z., Wang, S., Wu, J., & Zhou, W. (2022). Recent progress in defective TiO<sub>2</sub> photocatalysts for energy and environmental applications. *Renewable and Sustainable Energy Reviews*, 156, 111980. <https://doi.org/10.1016/j.rser.2021.111980>
- Limpachanangkul, P., Liu, L., Hunsom, M., Piumsomboon, P., & Chalermminsuan, B. (2022). Application of Bi<sub>2</sub>O<sub>3</sub>/TiO<sub>2</sub> heterostructures on glycerol photocatalytic oxidation to chemicals. *Energy Reports*, 8, 1076–1083. <https://doi.org/10.1016/j.egy.2022.07.131>
- Luo, H., Guo, J., Shen, T., Zhou, H., Liang, J., & Yuan, S. (2020). Study on the catalytic performance of LaMnO<sub>3</sub> for the RhB degradation. *Journal of the Taiwan Institute of Chemical Engineers*, 109, 15–25. <https://doi.org/10.1016/j.jtice.2020.01.011>
- Lv, X., Lam, F.L.-Y., & Hu, X. (2022). Developing SrTiO<sub>3</sub>/TiO<sub>2</sub> heterostructure nanotube array for photocatalytic fuel cells with improved efficiency and elucidating the effects of organic substrates. *Chemical Engineering Journal*, 427, 131602. <https://doi.org/10.1016/j.cej.2021.131602>
- Maurino, V., Bedini, A., Minella, M., Rubertelli, F., Pelizzetti, E., & Minerio, C. (2008). Glycerol Transformation Through Photocatalysis: A Possible Route to Value Added Chemicals. *Journal of Advanced Oxidation Technologies*, 11, 1203–8407. <https://doi.org/10.1515/jaots-2008-0201>
- Mavuso, M. A., Makgwane, P. R., & Ray, S. S. (2022). Construction of heterojunctions CeO<sub>2</sub> interfaced Nb, Sn, Ti, Mo and Zn metal oxide catalysts for photocatalytic oxidation of  $\alpha$ -pinene inert C-H. *Inorganic Chemistry Communication*, 137, 109199. <https://doi.org/10.1016/j.inoche.2022.109199>
- Miah, A. T. (2021). Chapter 11-Visible light responsive titania-based nanostructures for photocatalytic reduction of carbon dioxide. In P. N. Tri, H. Wu, T. A. Nguyen, S. Barnabé, & P. Bénard (Eds.), *Nanomaterials for CO<sub>2</sub> capture, storage, conversion and utilization* (pp. 239–266). Elsevier. <https://doi.org/10.1016/B978-0-12-822894-4.00009-5>
- Morawski, A. W., Kusiak-Nejman, E., Wanag, A., Narkiewicz, U., Edelmánová, M., Reli, M., & Kočí, K. (2021). Influence of the calcination of TiO<sub>2</sub>-reduced graphite hybrid for the photocatalytic reduction of carbon dioxide. *Catalysis Today*, 380, 32–40. <https://doi.org/10.1016/j.cattod.2021.05.017>
- Muniandy, S. S., Kaus, N. H. M., & Jiang, Z.-T. (2017). Altra-rawneh, M., Lee, H. L. Green synthesis of mesoporous anatase TiO<sub>2</sub> nanoparticles and their photocatalytic activities. *RSC Advances*, 7, 48083–48094. <https://doi.org/10.1039/C7RA08187A>



- Murphy, A. (2007). Band-gap determination from diffuse reflectance measurements of semiconductor films, and application to photoelectrochemical water-splitting. *Solar Energy Materials and Solar Cells*, *91*, 1326–1337. <https://doi.org/10.1016/j.solmat.2007.05.005>
- Mushtaq, K., Saeed, M., Gul, W., Munir, M., Firdous, A., Yousaf, T., Khan, K., Sarwar, H. M. R., Asad, M., & Zahid, S. (2020). Synthesis and characterization of TiO<sub>2</sub> via sol-gel method for efficient photocatalytic degradation of antibiotic ofloxacin. *Inorganic and Nano-Metal Chemistry*, *50*, 580–586. <https://doi.org/10.1080/24701556.2020.1722695>
- Noori, L., Hoseinpour, V., & Shariatinia, Z. (2022). Optimization of TiO<sub>2</sub> paste concentration employed as electron transport layers in fully ambient air processed perovskite solar cells with a low-cost architecture. *Ceramics International*, *48*, 320–336. <https://doi.org/10.1016/j.ceramint.2021.09.107>
- Ouerghi, O., Geesi, M. H., Ibnouf, E. O., Ansari, M. J., Alam, P., Elsanousi, A., Kaibaa, A., & Riadi, Y. (2021). Sol-gel synthesized rutile TiO<sub>2</sub> nanoparticles loaded with cardamom essential oil: Enhanced antibacterial activity. *Journal of Drug Delivery Science and Technology*, *64*, 102581. <https://doi.org/10.1016/j.jddst.2021.102581>
- Padmini, M., Balaganapathi, T., & Thilakan, P. (2021). Mesoporous rutile TiO<sub>2</sub>: Synthesis, characterization and photocatalytic performance studies. *Materials Research Bulletin*, *144*, 111480. <https://doi.org/10.1016/j.cci.2015.02.009>
- Payormhorm, J., Chuangchote, S., Kiatkittipong, K., Chirakorn, S., & Laosiripojana, N. (2017). Xylitol and gluconic acid productions via photocatalytic-glucose conversion using TiO<sub>2</sub> fabricated by surfactant-assisted techniques: Effects of structural and textural properties. *Materials Chemistry and Physics*, *196*, 29–36. <https://doi.org/10.1016/j.matchemphys.2017.03.058>
- Pelaez, M., Falaras, P., Likodimos, V., Kontos, A. G., de la Cruz, A. A., O'shea, K., & Dionysiou, D. D. (2010). Synthesis, structural characterization and evaluation of sol-gel-based NF-TiO<sub>2</sub> films with visible light-photoactivation for the removal of microcystin-LR. *Applied Catalysis, b: Environmental*, *99*, 378–387. <https://doi.org/10.1016/j.apcatb.2010.06.017>
- Phomma, S., Wutikhun, T., Kasamechonchung, P., Eksang-sri, T., & Sapcharoenkun, C. (2020). Effect of Calcination Temperature on Photocatalytic Activity of Synthesized TiO<sub>2</sub> Nanoparticles via Wet Ball Milling Sol-Gel Method. *Applied Sciences*, *10*, 993. <https://doi.org/10.3390/app10030993>
- Pica, M., Calzuola, S., Donnadio, A., Gentili, P., Nocchetti, M., & Casciola, M. (2018). De-Ethylation and Cleavage of Rhodamine B by a Zirconium Phosphate/Silver Bromide Composite Photocatalyst. *Catalysts*, *9*, 1–15. <https://doi.org/10.3390/catal9010003>
- Porto, S. P. S., Fleury, P. A., & Damen, T. C. (1967). Raman Spectra of TiO<sub>2</sub>, MgF<sub>2</sub>, ZnF<sub>2</sub>, FeF<sub>2</sub>, and MnF<sub>2</sub>. *Physical Review*, *154*, 522–526. <https://doi.org/10.1103/PHYSRE.154.522>
- Rahim, S., Ullah, R., Tuzen, M., Ullah, S., Sari, A., & Saleh, T. A. (2023). Synthesis of alumina-carbon framework for efficient sorption of methyl orange from wastewater with factorial design and mechanisms. *Groundwater for Sustainable Development*, *22*, 100950. <https://doi.org/10.1016/j.gsd.2023.100950>
- Reitz, C., Reinacher, J., Hartmann, P., & Brezesinski, T. (2014). Polymer-templated ordered large-pore mesoporous anatase-rutile TiO<sub>2</sub>: Ta nanocomposite films: Microstructure, electrical conductivity, and photocatalytic and photoelectrochemical properties. *Catalysis Today*, *225*, 55–63. <https://doi.org/10.1016/j.cattod.2013.09.017>
- Roongraung, K., Chuangchote, S., & Laosiripojana, N. (2020). Enhancement of Photocatalytic Oxidation of Glucose to Value-Added Chemicals on TiO<sub>2</sub> Photocatalysts by A Zeolite (Type Y) Support and Metal Loading. *Catal*, *10*, 423. <https://doi.org/10.3390/catal10040423>
- Saif, M., Aboul-Fotouh, S. M. K., El-Molla, S. A., Ibrahim, M. M., & Ismail, L. F. M. (2010). Improvement of the structural, morphology, and optical properties of TiO<sub>2</sub> for solar treatment of industrial wastewater. *J. Nanoparticle Res*, *14*, 101–111. [https://doi.org/10.1007/978-3-319-05041-6\\_8](https://doi.org/10.1007/978-3-319-05041-6_8)
- Saikumari, N., Dev, S. M., & Dev, S. A. (2021). Effect of calcination temperature on the properties and applications of bio extract mediated titania nano particles. *Science and Reports*, *11*, 1734. <https://doi.org/10.1038/s41598-021-80997-z>
- Santos, L. M., Da Silva, D. J. R., & Machado, A. E. H. (2021). Effect of time of hydrothermal heat treatment on mesoporous nano-TiO<sub>2</sub> synthesis. *Ceramics*, *67*, 445–454. <https://doi.org/10.1590/0366-69132021673843084>
- Sarngan, P. P., Lakshmanan, A., & Sarkar, D. (2022). Influence of Anatase-Rutile Ratio on Band Edge Position and Defect States of TiO<sub>2</sub> Homojunction Catalyst. *Chemosphere*, *286*, 131692. <https://doi.org/10.1016/j.chemosphere.2021.131692>
- Scheinost, A. C. (2005). METAL OXIDES. Encyclopedia of Soils in the Environment, ed by Hillel, D. Elsevier. pp. 428–438. <https://doi.org/10.1016/b0-12-348530-4/00194-6>
- Selman, A. M., & Husham, M. (2016). Calcination induced phase transformation of TiO<sub>2</sub> nanostructures and fabricated a Schottky diode as humidity sensor based on rutile phase. *Sensing and Bio-Sensing Research*, *11*, 8–13. <https://doi.org/10.1016/j.sbsr.2016.09.003>
- Senthilkumar, S., Ashok, M., Kashinath, L., Sanjeeviraja, C., & Rajendran, A. (2017). Phytosynthesis and Characterization of TiO<sub>2</sub> Nanoparticles using Diospyros ebenum Leaf Extract and their Antibacterial and Photocatalytic Degradation of Crystal Violet. *Smart Science*, *6*, 1–9. <https://doi.org/10.1080/23080477.2017.1410012>
- Shah, A. H., & Rather, M. A. (2021a). Effect of calcination temperature on the crystallite size, particle size and zeta potential of TiO<sub>2</sub> nanoparticles synthesized via polyol-mediated method. *Materials Today: Proceedings*, *44*, 482–488. <https://doi.org/10.1016/j.matpr.2020.10.199>
- Shah, A. H., & Rather, M. A. (2021b). Effect of Thermal Treatment on the Phase Composition and Surface Properties of WO<sub>3</sub>-TiO<sub>2</sub> Nanocomposites Synthesized via Hydro-Thermal Method. *ChemistrySelect*, *6*, 987–994. <https://doi.org/10.1002/slct.202004160>
- Shandilya, P., Sambnam, S., Sharma, R., Mandyal, P., & Fang, B. (2022). Properties, optimized morphologies,

- and advanced strategies for photocatalytic applications of  $\text{WO}_3$  based photocatalysts. *Journal of Hazardous Materials*, 428, 128218. <https://doi.org/10.1016/j.jhazmat.2022.128218>
- Sharma, S., Mittal, A., Chauhan, N. S., Saini, S., Yadav, J., Kushwana, M., Chakraborty, R., Sengupta, S., Kumari, K., & Kumar, N. (2022). Mechanistic investigation of RhB photodegradation under low power visible LEDs using a Pd-modified  $\text{TiO}_2/\text{Bi}_2\text{O}_3$  photocatalyst: Experimental and DFT studies. *Journal of Physics and Chemistry of Solids*, 162, 110510. <https://doi.org/10.1016/j.jpics.2021.110510>
- Sienkiewicz, A., Wanag, A., Kusiak-Nejman, E., Ekiert, E., Rokicka-Konieczna, P., & Morawski, A. W. (2021). Effect of calcination on the photocatalytic activity and stability of  $\text{TiO}_2$  photocatalysts modified with APTES. *Journal of Environmental Chemical Engineering*, 9, 104794. <https://doi.org/10.1016/j.jece.2020.104794>
- Singh, J., Sahu, K., Satpati, B., & Mohapatra, S. (2019). Facile synthesis, structural, optical and photocatalytic properties of anatase/rutile mixed phase  $\text{TiO}_2$  ball-like sub-micron structures. *Optik*, 118, 270–276. <https://doi.org/10.1016/j.jijleo.2019.05.053>
- Torres-Olea, B., Mérida-Morales, S., García-Sancho, C., Cecilia, J. A., & Maireles-Torres, P. (2020). Catalytic Activity of Mixed  $\text{Al}_2\text{O}_3\text{-ZrO}_2$  Oxides for Glucose Conversion into 5-Hydroxymethylfurfural. *Catal*, 10, 878. <https://doi.org/10.3390/catal10080878>
- Tuzen, M., Sari, A., & Saleh, T. A. (2018). Response surface optimization, kinetic and thermodynamic studies for effective removal of rhodamine B by magnetic AC/CeO<sub>2</sub> nanocomposite. *Journal of Environmental Management*, 206, 170–177. <https://doi.org/10.1016/j.jenvman.2017.10.016>
- Ullah, R., Naeemullah, Tuzen, & M. (2023). Photocatalytic removal of organic dyes by titanium doped alumina nanocomposites: Using multivariate factorial and kinetics models. *Journal of Molecular Structure*, 1285, 135509. <https://doi.org/10.1016/j.molstruc.2023.135509>
- Vequizo, J. J. M., Matsunaga, H., Ishiku, T., Kamimura, S., Ohno, T., & Yamakata, A. (2017). Trapping-Induced Enhancement of Photocatalytic Activity on Brookite  $\text{TiO}_2$  Powders: Comparison with Anatase and Rutile  $\text{TiO}_2$  Powders. *ACS Catalysis*, 7, 2644–2651. <https://doi.org/10.1021/acscatal.7b00131>
- Wang, X., Wu, G., Zhang, X., Wang, D., Lan, J., & Li, J. (2019). Selective Oxidation of Glycerol to Glyceraldehyde with  $\text{H}_2\text{O}_2$  Catalyzed by CuNiAl Hydrotalcites Supported BiOCl in Neutral Media. *Catal. Letters*, 149, 1046–1056. <https://doi.org/10.1007/s10562-019-02689-8>
- Watanabe, T., Takizawa, T., & Honda, K. (1977). Photocatalysis through excitation of adsorbates. I. Highly efficient N-deethylation of rhodamine B adsorbed to cadmium sulfide. *Journal of Physical Chemistry*, 81, 1845–1851. <https://doi.org/10.1021/j100534a012>
- Winter, M., Hamal, D., Yang, X., Kwen, H., Jones, D., Rajagopalan, S., & Klabunde, K. J. (2009). Defining Reactivity of Solid Sorbents: What Is the Most Appropriate Metric? *Chemistry of Materials*, 21, 2367–2374. <https://doi.org/10.1021/cm8032884>
- Wood, D. L., & Tauc, J. (1972). Weak Absorption Tails in Amorphous Semiconductors. *Physical Review B*, 5, 3144–3151. <https://doi.org/10.1103/PhysRevB.5.3144>
- Xu, D., & Ma, H. (2021). Degradation of rhodamine B in water by ultrasound-assisted  $\text{TiO}_2$  photocatalysis. *Journal of Cleaner Production*, 313, 127758. <https://doi.org/10.1016/j.jclepro.2021.127758>
- Xue, S., Wu, C., Pu, S., Hou, Y., Tong, T., Yang, G., Qin, Z., Wang, Z., & Bao, J. (2019). Direct Z-Scheme charge transfer in heterostructured  $\text{MoO}_3/\text{g-C}_3\text{N}_4$  photocatalysts and the generation of active radicals in photocatalytic dye degradations. *Environmental Pollution*, 250, 338–345. <https://doi.org/10.1016/j.envpol.2019.04.010>
- Yin, H., Wang, Y., Ma, L., Zhang, S., Yang, B., & Jiang, R. (2022). Effect of surface-deposited  $\text{Ti}_3\text{C}_2\text{T}_x$  MXene on the photoelectrochemical water-oxidation performance of iron-doped titania nanorod array. *Chemical Engineering Journal*, 431, 134124. <https://doi.org/10.1016/j.cej.2021.134124>
- Yoon, Y., Truong, P. P., Lee, D., & Ko, S. H. (2022). Metal-Oxide Nanomaterials Synthesis and Applications in Flexible and Wearable Sensors. *ACS Nano*, 2, 64–92. <https://doi.org/10.1021/acsnanoscienceau.1c00029>
- Yu, J., Dappozze, F., Martín-Gomez, J., Hidalgo-Carrillo, J., Marinas, A., Vernoux, P., & Guillard, C. (2021). Glyceraldehyde production by photocatalytic oxidation of glycerol on  $\text{WO}_3$ -based materials. *Applied Catalysis B: Environmental*, 299, 120616. <https://doi.org/10.1016/j.apcatb.2021.120616>
- Yuangpho, N., Le, S. T. T., Treerujiraphong, T., Khanitchaidecha, W., & Nakaruk, A. (2015). Enhanced photocatalytic performance of  $\text{TiO}_2$  particles via effect of anatase–rutile ratio. *Physica E: Low-Dimensional Systems and Nanostructures*, 67, 18–22. <https://doi.org/10.1016/j.physe.2014.11.006>
- Zelekew, O. A., Fufa, P. A., Sabir, F. K., & Duma, A. D. (2021). Water hyacinth plant extract mediated green synthesis of  $\text{Cr}_2\text{O}_3/\text{ZnO}$  composite photocatalyst for the degradation of organic dye. *Heliyon*, 07, e07652. <https://doi.org/10.1016/j.heliyon.2021.e07652>
- Zerjav, G., Žižek, K., Zavašnik, J., & Pintar, A. (2022). Brookite vs. rutile vs. anatase: What's behind their various photocatalytic activities? *Journal of Environmental Chemical Engineering*, 10, 107722. <https://doi.org/10.1016/j.jece.2022.107722>
- Zhang, J., Zhou, P., Liu, J., & Yu, J. (2014). New understanding of the difference of photocatalytic activity among anatase, rutile and brookite  $\text{TiO}_2$ . *Physical Chemistry Chemical Physics: PCCP*, 16, 20382–20386. <https://doi.org/10.1039/C4CP02201G>
- Zhang, Q., Du, J., He, A., Liu, Z., & Tao, C. (2019). High-selectivity electrochemical conversion of  $\text{CO}_2$  to lower alcohols using a multi-active sites catalyst of transition-metal oxides. *Journal of CO<sub>2</sub> Utilization*, 34, 635–645. <https://doi.org/10.1016/j.jcou.2019.08.005>
- Zhang, W., He, H., Tian, Y., Lan, K., Liu, Q., Wang, C., Liu, Y., Elzatahry, A., Che, R., Li, W., & Zhao, D. (2019b). Synthesis of Uniform Ordered Mesoporous  $\text{TiO}_2$  Microspheres with Controllable Phase Junctions for Efficient Solar Water Splitting. *Chemical Science*, 10, 1664–1670. <https://doi.org/10.1039/C8SC04155E>

- Zhang, F., Feng, G., Hu, M., Huang, Y., & Zeng, H. (2020). Liquid-Plasma Hydrogenated Synthesis of Gray Titania with Engineered Surface Defects and Superior Photocatalytic Activity. *Nanomaterials*, *10*, 342. <https://doi.org/10.3390/nano10020342>
- Zhang, X., Kamali, M., Uleners, T., Symus, J., Zhang, S., Liu, Z., Costa, M. E. V., Appels, L., Cabooter, D., & Dewil, R. (2022). UV/TiO<sub>2</sub>/periodate system for the degradation of organic pollutants – Kinetics, mechanisms and toxicity study. *Chemical Engineering Journal*, *449*, 137680. <https://doi.org/10.1016/j.cej.2022.137680>
- Zhao, S., Dai, Z., Guo, W., Chen, F., Liu, Y., & Chen, R. (2019). Highly Selective Oxidation of Glycerol over Bi/Bi<sub>3,64</sub>Mo<sub>0,36</sub>O<sub>6,55</sub> Heterostructure: Dual Reaction Pathways Induced by Photogenerated <sup>1</sup>O<sub>2</sub> and Holes. *Applied Catalysis, b: Environmental*, *244*, 206–214. <https://doi.org/10.1016/j.apcatb.2018.11.047>
- Zhuang, J., Dai, W., Tian, Q., Li, Z., Xie, L., Wang, J., Liu, P., Shi, X., & Wang, D. (2010). Photocatalytic Degradation of RhB over TiO<sub>2</sub> Bilayer Films: Effect of Defects and Their Location. *Langmuir*, *26*, 9686–9694. <https://doi.org/10.1021/la100302m>

**Publisher's Note** Springer Nature remains neutral with regard to jurisdictional claims in published maps and institutional affiliations.

Springer Nature or its licensor (e.g. a society or other partner) holds exclusive rights to this article under a publishing agreement with the author(s) or other rightsholder(s); author self-archiving of the accepted manuscript version of this article is solely governed by the terms of such publishing agreement and applicable law.